# Josephson Array-Mode Parametric Amplifier

V. V. Sivak,[1,*] S. Shankar,[1,†] G. Liu,[1] J. Aumentado,[2] and M. H. Devoret[1]

[1] *Department of Applied Physics, Yale University, New Haven, Connecticut 06520, USA*

[2] *National Institute of Standards and Technology, Boulder, Colorado 80305, USA*

(Received 23 September 2019; accepted 20 December 2019; published 7 February 2020)

We introduce a near-quantum-limited amplifier with a large tunable bandwidth and high dynamic range—the Josephson array-mode parametric amplifier (JAMPA). The signal and idler modes involved in the amplification process are realized by the array modes of a chain of 1000 flux-tunable Josephson-junction-based nonlinear elements. The frequency spacing between the array modes is comparable to the flux tunability of the modes, ensuring that any desired frequency can be occupied by a resonant mode, which can further be pumped to produce high gain. We experimentally demonstrate that the device can be operated as a nearly quantum-limited parametric amplifier with 20 dB of gain at almost any frequency within a 4–12-GHz band. On average, it has a 3-dB bandwidth of 11 MHz and an input 1-dB compression power of −108 dBm, which can go as high as −93 dBm. We envision the application of such a device to the time- and frequency-multiplexed readout of multiple qubits, as well as to the generation of continuous-variable cluster states.

DOI: 10.1103/PhysRevApplied.13.024014

## I. INTRODUCTION

Quantum-limited parametric amplifiers have become necessary tools for quantum measurements involving readout at microwave frequencies. The improved signal-to-noise ratio brought about by these amplifiers is crucial in applications such as real-time feedback in quantum error correction [1,2] but also simply in quantum benchmarking experiments such as qubit lifetime characterization in superconducting circuits [3,4]. These devices are also used as sources of squeezing for enhancement of detection sensitivity [5,6], and sources of entanglement in continuous-variable quantum computing [7,8].

The most common implementations of nearly quantum-limited parametric amplifiers are based on nonlinear resonators containing Josephson junctions (JJs), such as Josephson parametric amplifiers (JPAs) [9,10] and converters [11,12]. These resonant amplifiers have a limited bandwidth and dynamic range, and work in reflection, therefore requiring commercial circulators for signal routing. In contrast, traveling-wave parametric amplifiers (TWPAs) based on Josephson junctions [13–18] or high-kinetic-inductance materials [19–23] are broadband, have a higher dynamic range, and are, in principle, directional. In recent years, Josephson TWPAs have become practical and have been widely adopted in the field [5,24–27], despite the fabrication challenges involved in attaining impedance matching and resonant phase matching.

However, TWPAs have failed to achieve one of their original promises, namely directionality. For high-coherence superconducting qubits, an extremely clean electromagnetic environment is crucial. This would be compromised if the TWPAs were used without an isolator at the input port, since the reflected strong pump and amplified signal and quantum noise would travel back to the qubits and cause unwanted back action. Such reflections happen due to small impedance mismatches, which are inevitably present within the large bandwidth of a TWPA. In practice, to operate a TWPA, isolators are also essential for impedance matching of the input port. Operating a TWPA in such a setting is therefore equivalent to operating a broadband high-dynamic-range *reflection amplifier*.

This observation naturally leads to the following question: by dropping the directionality constraint, is it possible to construct a reflection amplifier which avoids the two most strict and challenging requirements for a TWPA, namely (i) impedance matching and (ii) phase matching, and at the same time is significantly better than commonplace resonant reflection amplifiers in terms of the bandwidth and dynamic range?

In this paper, we achieve a more modest goal as a step toward answering this question. We construct an amplifier with the following characteristics: (i) its flux-tunable bandwidth is larger than the dynamic bandwidth of a

*sivak.volodymyr@gmail.com

†Current address: Department of Electrical and Computer Engineering, University of Texas at Austin, Austin, Texas 78712, USA.

 

Josephson TWPA, (ii) its dynamic range is comparable to that of a Josephson TWPA, with $P_{1\,\mathrm{dB}}^{\mathrm{average}} = -108$ dBm and $P_{1\,\mathrm{dB}}^{\mathrm{best}} = -93$ dBm, and (iii) its added-noise performance matches that of state-of-the-art near-quantum-limited resonant amplifiers. The basic idea behind the device is to harness the collection of modes of a nonlinear Fabry-Perot resonator, realized as a long array of flux-tunable nonlinear Josephson mixing elements, hence the name Josephson array-mode parametric amplifier (JAMPA). If the frequency spacing between the array modes is smaller than the flux tunability of the modes, then any desired frequency can be occupied by a resonant mode at a certain flux, which can further be pumped to produce gain. In practice, the tunable bandwidth of such a device is essentially limited by the 4–12-GHz bandwidth of our cryogenic measurement chain.

To get access to three-wave mixing and potential *in situ* Kerr suppression [28], we choose to use an array of superconducting nonlinear asymmetric inductive elements (SNAILs) [29], although it is possible to make a JAMPA with other types of flux-tunable mixing elements, such as dc or rf superconducting quantum interference devices (SQUIDs). We note that, in parallel with this work, a similar idea was developed in Ref. [30], where pairs of modes (dimers) of two coupled arrays of SQUIDs are utilized for amplification.

The remainder of this paper is organized as follows: in Sec. II, we study the effect of the array size on various amplifier properties, demonstrating how increasing the size naturally leads to the idea of the JAMPA. In Sec. III, we present an experimental comparison of several devices with array sizes of 20, 200, and 1000. In Sec. IV, we characterize the performance of the JAMPA. We conclude and discuss possible applications and future directions in Sec. V.

## II. EFFECT OF ARRAY SIZE ON AMPLIFIER MODE STRUCTURE AND NONLINEARITY

To approach the question posed in the Introduction, we start by exploring what phenomena limit the dynamic range in Josephson parametric amplifiers and how these effects can be mitigated. The two dominant physical mechanisms that are understood to cause the saturation of parametric amplifiers are (i) signal-induced Stark shifts that detune the amplifier from its operating point and (ii) depletion of pump photons due to signal amplification. The former was shown to be the dominant factor in the saturation of resonant amplifiers [28,29,31,32], and some evidence indicates that it might also cause the saturation of TWPAs [18,33]. The spurious Stark shift originates from the quartic Kerr nonlinearity of the resonator hosting the amplification process, and therefore the path toward improved dynamic range requires the suppression of this nonlinearity while still preserving the mixing capability.

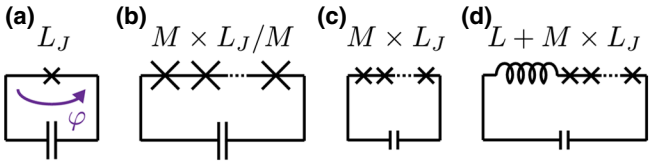


FIG. 1. (a) Simple circuit model of a JPA resonator: a junction with inductance $L_J$ shunted with a capacitance $C$. (b) Arraying of $M$ junctions with an inductance $M$ times smaller. (c) Arraying of $M$ identical junctions requires a smaller capacitance to keep the resonance frequency constant. (d) Array in series with geometric inductance.

One promising direction for suppression of the Kerr nonlinearity, suggested in Ref. [34], is to replace the single mixing element, such as a Josephson junction, with an array, to distribute the power-handling load among many junctions. In this section, we revisit this idea of arraying.

Consider first a simple model of a JPA resonator, shown in Fig. 1(a), consisting of a single Josephson junction with a Josephson energy $E_J$ (and an inductance $L_J$), capacitively shunted with a capacitance $C$. Let $\varphi = \varphi_{\mathrm{ZPF}}(a + a^\dagger)$ denote the superconducting phase across the junction, where $\varphi_{\mathrm{ZPF}} = \sqrt{Z_a/2R_q}$ is the amplitude of the zero-point fluctuations (ZPF) of the phase, defined by the ratio of the mode impedance $Z_a$ to the superconducting resistance quantum $R_q = \hbar/(2e)^2$. The Hamiltonian of such a circuit is $\mathcal{H} = (2eN)^2/2C - E_J \cos\varphi$, where $N$ is the number of Cooper pairs that have tunneled across the junction. We consider the limit of small $\varphi_{\mathrm{ZPF}}$, where the cosine expansion is valid, and truncate it at the fourth order, obtaining a weakly anharmonic oscillator with resonant frequency $\omega_a$.

The quartic contribution $E_J\varphi^4/4!$ to the Hamiltonian, also referred to as the Kerr nonlinearity, can be diluted by replacing a single junction with an array of $M$ junctions each having a Josephson energy $M$ times higher (and an inductance $M$ times smaller), as shown in Fig. 1(b). Then, in the lowest-energy configuration, the phase $\varphi$ is split equally among the junctions, and the quartic contribution to the Hamiltonian becomes

$$\frac{ME_J}{4!}\sum_{i=1}^{M}\left(\frac{\varphi}{M}\right)^4 = \frac{E_J}{4!}\frac{\varphi_{\mathrm{ZPF}}^4}{M^2}(a^\dagger + a)^4 \propto \frac{1}{M^2}. \quad (1)$$

Importantly, in such an approach to arraying, the resonant frequency and the impedance of the JPA remain independent of $M$.

In practice, however, this approach is not feasible due to the difficulty in fabricating junctions with an increasingly large Josephson energy $ME_J$ as the array size is increased. A more realistic and practical approach is to array fixed-$E_J$ junctions with the largest critical current that can be reliably reproduced in a fabrication process, as shown in Fig. 1(c). In this case the mode inductance

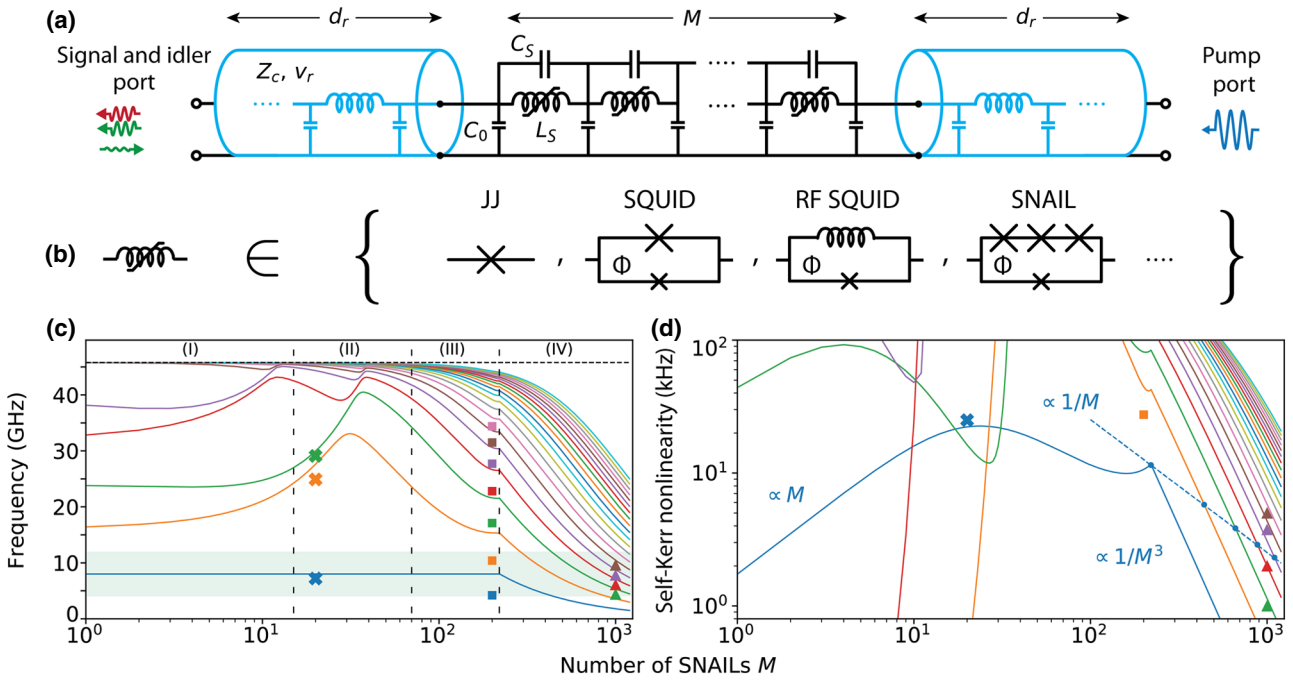


FIG. 2. (a) Distributed circuit model of the type of parametric amplifier considered in this paper. An array of $M$ unit cells, comprising a nonlinear inductance $L_S$ and capacitances $C_0$ and $C_S$, embedded into a transmission-line resonator of characteristic impedance $Z_c$ and phase velocity $v_r$. (b) Superconducting circuit elements that can provide a nonlinear inductance $L_S$. (c) Resonant frequencies and (d) self-Kerr nonlinearities of the modes of this structure with a SNAIL at $\Phi = 0$ as a nonlinear inductor. For each $M$, the resonator length $2d_r$ is adjusted to keep the fundamental mode of the structure at a fixed frequency. Past a certain critical $M$, the resonator leads shrink to size zero (region IV). The solid curves are calculated for parameters of the system which are typical for our fabrication method (see Appendix B); their color encodes the mode number. The data points correspond to devices A (crosses), B (squares), and C (triangles) and are shown for reference; they are not expected to precisely line up with the theoretical curves. The 4–12-GHz strip denotes the accessible frequency window in which modes can be directly identified using the reflection measurement. Two-tone spectroscopy is used to locate the resonances outside this window. The self-Kerr nonlinearities in (d) are measured using IMD spectroscopy (see text). The vertical dashed lines in (c) denote approximate boundaries where qualitative changes occur in the mode structure of the amplifier.

grows in proportion to $M$ (if the stray geometric inductance can be neglected), and therefore the capacitance has to be adjusted in proportion to $1/M$ in order to keep the working frequency the same. This, however, leads to an increase in the mode impedance proportional to $M$ and a corresponding increase in $\varphi_{\mathrm{ZPF}}$ proportional to $\sqrt{M}$. The last factor significantly affects the ability to dilute the Kerr nonlinearity:

$$\frac{E_J}{4!}\sum_{i=1}^{M}\left(\frac{\varphi}{M}\right)^4 = \frac{E_J}{4!}\frac{\varphi_{\mathrm{ZPF}}^4}{M^3}(a^\dagger + a)^4 \propto \frac{1}{M}. \qquad (2)$$

Furthermore, in practice there is often a linear inductance $L$ in series with the array, as shown in Fig. 1(d). This may be, for example, the stray geometric inductance of the leads or the intentionally fabricated inductance of the embedding circuit. For junctions with a large critical current such that $p_J \equiv L_J/L \ll 1$ and a small array size such that $Mp_J \ll 1$, the phase drop across each junction $\varphi \times p_J/(1 + Mp_J) \approx p_J\varphi$ is independent of $M$. In such arrays, the Kerr nonlinearity actually increases in proportion to $M$, as shown below:

$$\frac{E_J}{4!}\sum_{i=1}^{M}(p_J\varphi)^4 = \frac{E_J}{4!}M(p_J\varphi_{\mathrm{ZPF}})^4(a^\dagger + a)^4 \propto M. \qquad (3)$$

These simple scaling arguments demonstrate that a larger array size $M$ is not strictly equivalent to a smaller Kerr nonlinearity. To be more quantitative in support of this claim, we consider an analytical model that reflects a practically feasible approach to the arraying of nonlinear elements and avoids the multiple approximations involved in Eqs. (1)–(3). In this model, a unit cell of the array comprises a nonlinear inductance $L_S$, a capacitance to ground $C_0$, and a shunting capacitance $C_S$, as shown in Fig. 2(a). The inductance $L_S$ can come from any superconducting circuit element, such as a Josephson junction, a SQUID, or a SNAIL, as shown in Fig. 2(b). The array is embedded into a transmission-line resonator, isolated from the environment for simplicity of the analysis. The two arms of the

transmission-line resonator are of length $d_r$ each, and have a characteristic impedance $Z_c$ and phase velocity $v_r$.

As a distributed element, this system can support multiple standing electromagnetic modes. When $M$ is increased, the length $d_r$ is adjusted to keep the resonant frequency of the fundamental mode fixed. These conditions reflect the real constraints encountered in amplifier design. For this model, in Appendix B we perform an eigenmode decomposition and find the resonant frequency and self-Kerr nonlinearity of each mode as a function of the array size $M$. The result of such a calculation is plotted in Figs. 2(c) and 2(d) for realistic system parameters and with the choice of the nonlinear inductance as a SNAIL at $\Phi = 0$. For numerical analysis, we use a fundamental-mode frequency of 8 GHz, a SNAIL linear inductance $L_S = 110$ pH, distributed capacitances $C_0 = 0.71$ fF and $C_S = 0.11$ pF, a resonator characteristic impedance $Z_c = 46\ \Omega$, and a phase velocity $v_r = 1.2 \times 10^8$ m/s.

As can be seen from Fig. 2(c), the resonant frequency of the fundamental mode stays constant for $M < 220$ by construction. At small $M$, in region I, the higher modes of the structure approximately follow the dimensional quantization law for a $\lambda/2$-type transmission-line resonator, where the resonances are arranged with a spacing approximately equal to the frequency of the fundamental mode. The higher resonances bunch up tightly below the "plasma frequency" of the unit cell $\omega_p = 1/\sqrt{L_S C_S}$ [35,36]. The self-Kerr nonlinearity, as seen from Fig. 2(d), grows like $M$, in agreement with the qualitative discussion leading to Eq. (3). In region II, of intermediate $M$, where the inductive energy participation ratio (EPR) [37] of the array saturates at 1, the array acts as a superinductance [35,36] and the transmission-line leads contribute only to the capacitance. In this case the resonator is well approximated as a single lumped $LC$-type resonance, with all higher modes being pushed up in frequency. Further increase of $M$, in region III, results in a growing contribution of the distributed capacitance $C_0$ of the array, and the array modes descend in frequency. The scaling of the Kerr nonlinearity with $M$ in regions II and III changes to approximately $1/M^\gamma$, with $\gamma \approx 0.6$ for our choice of parameters, in contrast to the simplistic prediction of Eq. (2), due to the increased role of the distributed capacitance of the array. Eventually, after the critical value $M = 220$ is reached, the resonator leads shrink to zero, and we lose the knob that ensures that the frequency of the fundamental mode remains constant. For $M > 220$, corresponding to region IV, increasing the array size results in a $1/M$ scaling of the mode spacing. The self-Kerr nonlinearity of the fundamental mode is very efficiently diluted as $1/M^3$ in region IV, but its resonant frequency is pulled down, and therefore the fundamental mode cannot be used if the desired operating frequency is fixed. In this case one would have to use higher array modes that occupy the desired operating frequency. Taking this into account, the effective scaling of the self-Kerr nonlinearity goes only as $1/M$, as depicted in Fig. 2(c) by a dashed line.

Notably, this dependence on $M$ remains extremely weak, and the Kerr nonlinearity of the fundamental mode varies by only about a factor of two in the large range of $M \in [5,200]$. We believe that such a weak dependence accounts for the fact that arraying has not brought significant improvements of the dynamic range of parametric amplifiers, despite the significant effort in this direction by the community. For instance, amplifiers made with arrays of 8 SQUIDs [38], 80 SQUIDs [32], and 20 SNAILs [29] have dynamic ranges comparable to or worse than that of a device consisting of just a single SQUID [39]. For such a comparison to be fair fabricationwise, we note that the critical currents of the junctions used in all these designs are comparable and lie in the range 1–3 $\mu$A. Moreover, the dynamic range of Josephson TWPAs [14,18] with $M > 2000$ is close to what can be achieved with resonant amplifiers with $M = 20$ and careful choice of operating conditions [28], and is only one order of magnitude above the best performance of a *single* SQUID [39] (despite having three orders of magnitude more junctions). Such a comparison underlines the issue that arraying does not efficiently dilute the nonlinearity.

## III. ARRAY MODE FREQUENCIES AND KERR NONLINEARITIES: EXPERIMENT

In order to confirm our understanding of the scaling with $M$, we fabricate and test three devices, named A, B, and C, with $M \in \{20, 200, 1000\}$, varying on a logarithmic scale. From Figs. 2(c) and 2(d), we see that these devices should have mode structures characteristic of regions II, III, and IV, respectively.

The devices are fabricated in a single lithography step with a microstrip geometry on a 300-$\mu$m-thick silicon substrate. The ground plane is formed by a 2-$\mu$m-thick silver layer deposited on the back of the wafer. The Josephson junctions are formed by $Al/AlO_x/Al$ layers deposited using the Dolan bridge shadow evaporation process.

The devices are coupled to a 50 $\Omega$ environment via signal and pump ports, as illustrated in Fig. 2(a). The signal port is strongly coupled and sets the damping rate $\kappa \sim$ (150–250) MHz of the resonant modes. In devices A and B this coupling is capacitive, while in device C it is galvanic. The galvanic coupling of device C changes its mode structure compared with the model discussed in Sec. II, but does not affect the major results of this work, such as the scaling of the nonlinearity with $M$. Such a coupling is a necessary design choice to achieve a large $\kappa$ in device C. The pump port in each device is weakly capacitively coupled to a dedicated pump line. The device properties are summarized in Appendix A. To characterize them, we first measure the resonant-mode structure.

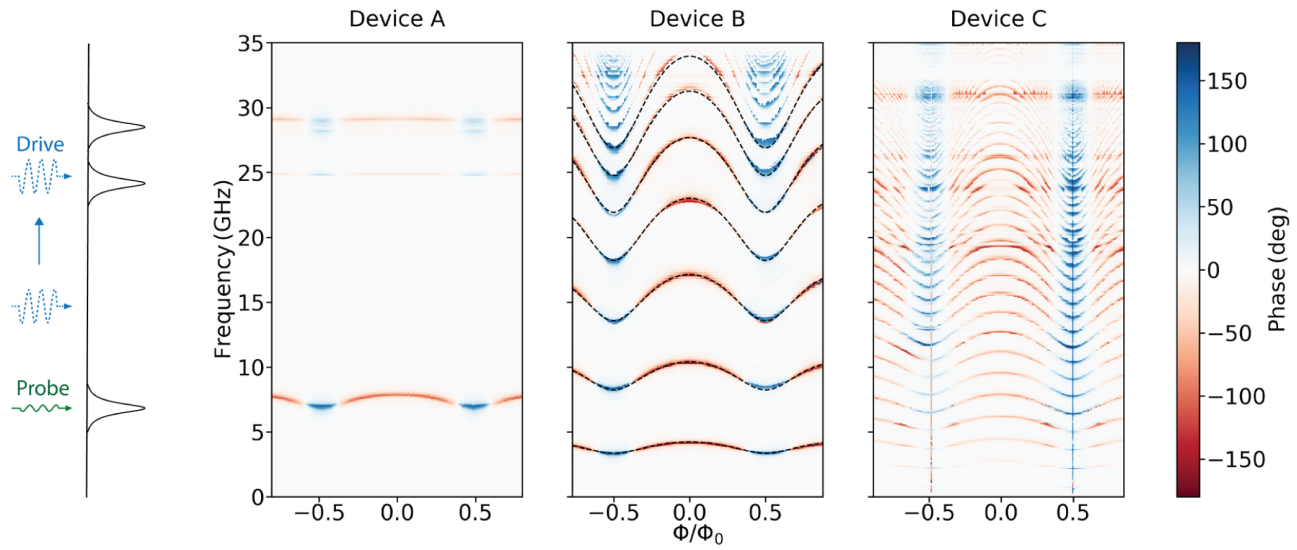


FIG. 3. Two-tone spectroscopy (background subtracted) of three devices with $M = 20$, 200, and 1000. The frequency landscape of the measurement is sketched on the left. A weak tone (green) is used to probe the phase at the resonance of one of the modes that fall within the measurement band of our setup. A strong drive tone (blue) is swept in frequency. When the drive crosses some resonance of the structure, the Stark shift of the monitored mode due to the self- or cross-Kerr coupling results in a phase response of the probe tone. The dashed line in the middle panel is a fit to the device model.

The resonances can be located with two-tone spectroscopy [35,40]. The frequency landscape of such a measurement is sketched in Fig. 3 on the left. The first, weak tone (green) is used to probe the resonance of one of the modes that fall within the 4–12-GHz measurement band of our setup, depicted in Fig. 5. This tone is applied through the strongly coupled port of the device and measured in reflection. At the same time, the second, strong drive tone (blue), applied through the weakly coupled pump port, is swept in frequency (and in power, to compensate for increasing attenuation at higher frequencies). When the drive crosses some resonance of the structure, the Stark shift of a monitored mode due to the self- or cross-Kerr coupling results in a phase response of the probe tone. Moreover, the sign of the phase shift corresponds to the sign of the self- or cross-Kerr nonlinearity that causes this shift.

The measurement result shown in Fig. 3 demonstrates that device A, with $M = 20$, is indeed in the "lumped" regime, with all higher modes being pushed up in frequency, in agreement with expectations for region II in Fig. 2(c). Its performance as an amplifier was characterized in detail in Ref. [28].

Device B, with an intermediate $M = 200$, displays multiple array modes separated by about 5 GHz. The decreased mode spacing at higher frequencies is a hallmark of the approaching "plasma resonance" as explained in Sec. II. We fit the frequencies of the array modes of this device to extract the values of the distributed capacitances $C_S = 0.11$ pF and $C_0 = 0.70$ fF characteristic of our fabrication process, which agree well with the expected design parameters. At higher frequencies, the deviation from the model of Sec. II (dashed lines) is more apparent, which might arise from the long-range Coulomb interaction between the islands of the array, as explained in Ref. [40]. The second mode of device B behaves as a regular SNAIL parametric amplifier (SPA), and was used in an experiment [41] to perform a single-shot readout of Andreev levels in an InAs nanowire Josephson junction.

Device C has regularly spaced low-lying modes with $\Delta\omega \approx 1.5$ GHz. Because of the similar extent of frequency tunability with flux, the modes of device C are able to almost entirely cover the 4–12-GHz frequency range accessible with our measurement setup. The vertical lines of different color visible in the two-tone-spectroscopy data likely result from phase slips in the array when the flux crosses $\Phi = \pm\Phi_0/2$, where $\Phi_0 = h/2e$ is the superconducting magnetic flux quantum.

In addition to the mode frequencies of devices A–C, we measure the self-Kerr nonlinearities using intermodulation (IMD) spectroscopy [28,29,42]. The results are summarized in Table I and are shown for reference in Fig. 2(d); they confirm the theoretical expectations. In particular, we are able to reduce the Kerr nonlinearity by an order of magnitude in device C ($M = 1000$) over devices A and B ($M = 20$ and 200, respectively). Note that a similar suppression could be achieved in a device with $M = 1$ due to a lower participation ratio. However, this would come at the cost of a flux tunability of only about 100 MHz and an inability to pump this device for amplification.

Having experimentally demonstrated the effect of the array size on the mode structure of the device, we now focus on studying the properties of device C, belonging to region IV in Fig. 2(c). This region looks interesting for application to parametric amplification, although it has not been systematically explored from this perspective before. One example of such a multimode amplifier was characterized in Ref. [43], where it was demonstrated that two modes of the device can be used for degenerate and nondegenerate gain processes with near-quantum-limited added noise. Another example [30], developed independently and in parallel with our work, utilizes pairs of modes (dimers) of two coupled arrays of SQUIDs to realize a tunable nondegenerate four-wave-mixing amplifier.

## IV. CHARACTERIZATION OF JAMPA

In this section, we present a detailed characterization of device C as a parametric amplifier. The results of the measurements of various amplifier characteristics are summarized in Fig. 4. In this experiment, we attempt to obtain 20 dB of gain at regularly spaced operating frequencies separated by approximately 100 MHz within the 4–12 GHz range. As shown in Fig. 4(c), we are able to cover most of this range except for frequency pockets which are not occupied by any of the modes at any external magnetic flux $\Phi$. Note that these gaps would disappear if the array size was increased further, since the mode spacing decreases as $1/M$.

The measurement is done using an automated search algorithm, which for each desired operating frequency $\omega_{\rm op}$ identifies the flux $\Phi$ at which one of the modes, indexed by $n$, is at resonance near $\omega_{\rm op}$, so that $\omega_n \approx \omega_{\rm op}$. Then, for each combination of modes $(n, m)$, by pumping around $\omega_n + \omega_m$, the algorithm attempts to find the pump power $P_p$ and frequency $\omega_p$ that yield 20 dB of gain at $\omega_{\rm op}$. Thus, some of the gain curves in Fig. 4(c) correspond to

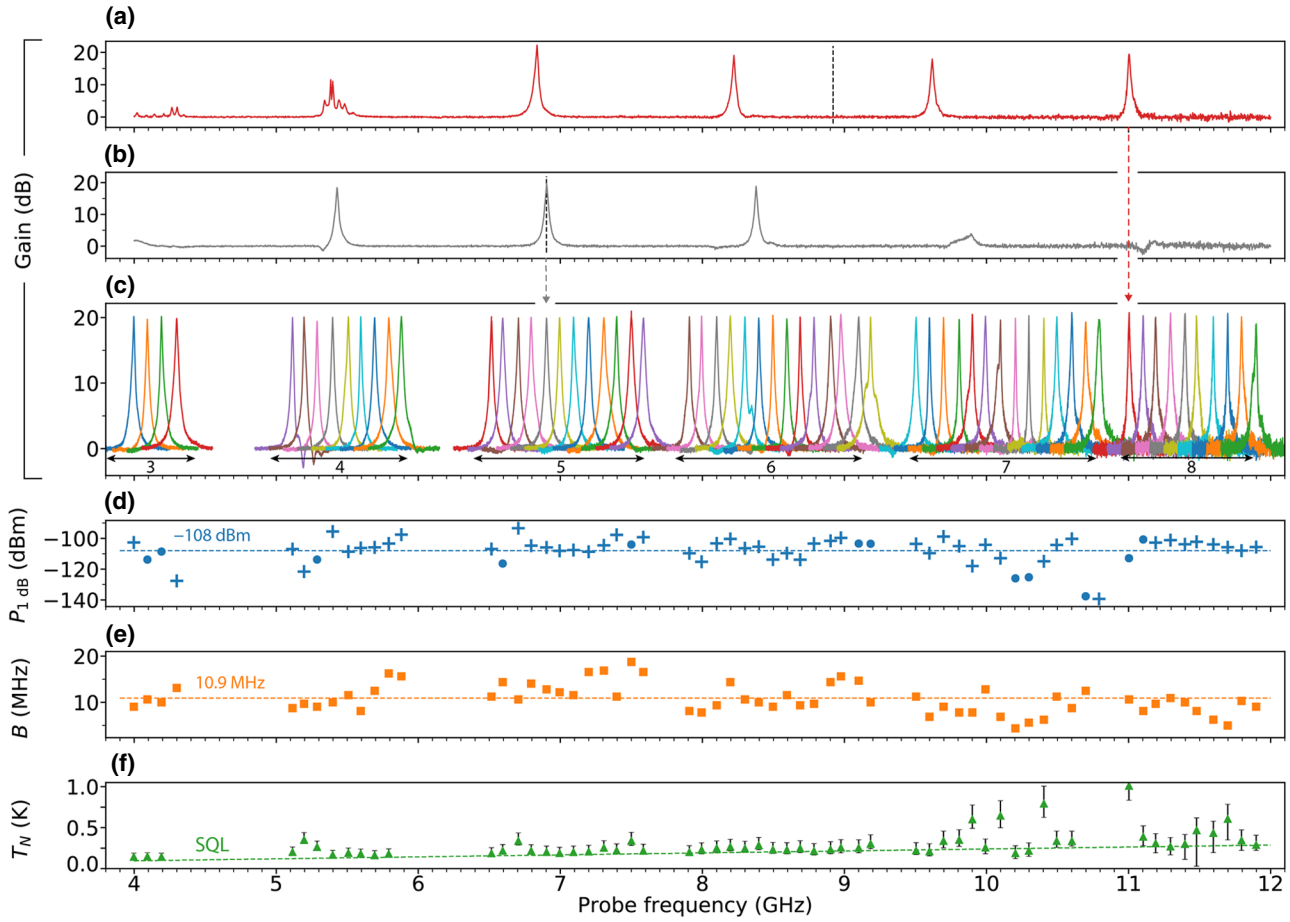


FIG. 4. (a) A single pump at $\omega_p = 2\pi \times 17.84$ GHz produces a large nondegenerate gain between two signal-idler pairs of modes. (b) A single pump at $\omega_p = 2\pi \times 13.81$ GHz produces large degenerate and nondegenerate gains. The vertical dashed line is located at $\omega_p/2$. (c) Demonstration of the wide flux tunability of the device. Each gain curve corresponds to a different pumping condition determined by $\Phi$, $\omega_p$, and $P_p$. The index of the mode used to produce gain is indicated at the bottom. (d) Saturation power, (e) 3 dB bandwidth, and (f) noise temperature, corresponding to the operating points shown in (c). The crosses and circles in (d) correspond to the −1-dB and +1-dB compression points, respectively [44], and we show only the lower of the two. The horizontal dashed lines in (d),(e) show the mean value; the sloped dashed line in (f) indicates the standard quantum limit $\hbar\omega/2k_B$.

a nondegenerate gain ($n \neq m$), as shown in Fig. 4(a), and some correspond to a degenerate gain ($n = m$), as shown in Fig. 4(b). The dashed lines in these panels indicate the location of $\omega_p/2$, which allows to identify if the gain curve is degenerate or nondegenerate. By looking at a wide frequency span, it is clear that the same pumping condition that yields $G = 20$ dB at the desired frequency $\omega_{\rm op}$, also yields a large gain in other modes that satisfy the frequency-matching condition $\omega_{n'} + \omega_{m'} = \omega_p$, resulting in a comblike gain profile.

For each operating condition in Fig. 4(c), we measure the 1-dB compression point $P_{1\ \rm dB}$, the 3-dB bandwidth $B$, and the noise temperature $T_N$, shown in Figs. 4(d)–4(f). On average, we obtain $B/2\pi = 10.9$ MHz and $P_{1\ \rm dB} = -108$ dBm, with some points as high as $-93$ dBm. This automated measurement is not optimized and reflects the average amplifier performance, but we expect that by careful fine-tuning of the controls (in particular, pump detuning [28,31]) an above-average performance can be obtained at most operating frequencies.

The added-noise temperature $T_N$ and 1-dB compression power $P_{1\ \rm dB}$ of the amplifier are calibrated using a shot-noise tunnel junction (SNTJ) [45,46], as explained in Appendix C. For a phase-preserving linear amplifier, the standard quantum limit (SQL) on the added noise, represented by a dashed line in Fig. 4(f), corresponds to $T_N = \hbar\omega/2k_B$. This half a photon of noise comes from the idler, whose presence is fundamentally necessary to preserve the commutation relations of the amplified operator, as stated by the Caves theorem [47]. As seen from Fig. 4(f), the JAMPA closely approaches this fundamental limit on the added noise over a wide range of frequencies, which has practical significance in the potential application of the JAMPA to qubit readout. More fundamentally, this agreement explicitly demonstrates the Caves theorem between 4 and 12 GHz. Note that some points above 9 GHz significantly deviate from the quantum limit, possibly due to the fact that the unselective pump might stimulate spurious conversion processes with unintended modes, leading to the existence of multiple idlers and increased added noise. Another possibility is multistability of the metapotential created by the parametric pump [28,48]. A more sophisticated tuning algorithm might resolve this problem.

Having characterized various aspects of the JAMPA, we move on to discussing its possible applications in circuit QED and ways to improve its performance.

## V. DISCUSSION AND CONCLUSION

From a practical point of view, the JAMPA demonstrates equally good performance over a broad tunable bandwidth, making it useful in experiments that require sequential rather than simultaneous measurements of multiple qubits. Fast flux lines or pump switching would be used for such sequential measurements of different channels [49]. Using a JAMPA in such a setting can save a large amount of space in a dilution refrigerator compared with using multiple narrow-band parametric amplifiers [50].

In addition, with further reduction of the mode spacing, the comblike gain profile of the JAMPA can become useful for frequency-division multiplexing [24,51–53] of multiple readout signals in a single amplifier. In this technique, to distribute the available bandwidth between multiple communication channels, it is optimal to arrange them at equally spaced frequencies, which makes it suitable for using a JAMPA.

We also envision more exotic applications of the JAMPA. For example, a squeezing comb can be used to generate continuous-variable cluster states [54], which are multimode entangled states that are resources for measurement-based universal quantum computation [55]. Such states can be constructed by coupling various modes of the JAMPA with squeezing and conversion pumps, as was demonstrated for tripartite entanglement generation in Ref. [8].

There is a lot of room for future investigation and improvement. The JAMPA is developed with the goal of using arraying to suppress the Kerr nonlinearity and thus enhance the dynamic range of the amplifier. As is evident from Fig. 1(b), the Kerr suppression is effective in this device, although $P_{1\ \rm dB}$ is not improved significantly over previous SNAIL parametric amplifiers. This is because the saturation power scales quadratically with the coupling rate $\kappa$, which is a few times smaller in the current device than in state-of-the-art SPAs. Increasing the coupling can be achieved in several ways, for example by lowering the characteristic impedance $Z_S = 390\ \Omega$ of the array. Since $\Delta\omega/\kappa = (\pi/2)Z_S/R$, lowering the impedance $Z_S$ can lead to a situation in which the comblike gain profile with multiple resolved peaks turns into a single broadband gain profile. Understanding this transition is an interesting theoretical problem. Notably, the idea behind a broadband parametric amplifier in Refs. [39,56] falls into the same category of using "blending" of multiple modes to enhance the dynamic bandwidth.

This brings us back to the question raised in the Introduction: is there an alternative to the TWPA, which achieves similar performance on important metrics, but has significantly smaller constraints on fabrication? We conjecture that the JAMPA in the "mode-blending" regime could potentially serve as such an alternative.

To conclude, we demonstrate how multiple array modes of a chain of tunable nonlinear mixing elements based on Josephson junctions can be used to dramatically enhance the tunable bandwidth of a Josephson parametric amplifier, while also achieving a state-of-the-art dynamic range and near-quantum-limited noise performance.

TABLE I. Parameters of the three devices studied in this experiment: number of SNAILs ($M$), inductance of the large junctions in the SNAIL ($L_J$), mode number ($n$), resonant frequency ($\omega_n$), coupling rate to the transmission line ($\kappa_n$), and self-Kerr nonlinearity ($K_n$) measured at $\Phi = 0$.

| Device | $M$ | $L_J$ (pH) | Mode, $n$ | $\omega_n/2\pi$ (GHz) | $\kappa_n/2\pi$ (MHz) | $K_n/2\pi$ (kHz) |
|---|---|---|---|---|---|---|
| A | 20 | 38 | 1 | 7.3 | 260 | 25.0 |
| B | 200 | 48 | 2 | 10.4 | 150 | 27.5 |
| C | 1000 | 48 | 3 | 4.4 | 150 | 1.0 |
| | | | 4 | 6.1 | 140 | 2.0 |
| | | | 5 | 7.8 | 140 | 3.7 |
| | | | 6 | 9.6 | 140 | 5.0 |


## ACKNOWLEDGMENTS

We acknowledge the contributions of N.E. Frattini, A. Lingenfelter, C. Ding, W. Dai, and S.O. Mundhada. J.A. wishes to acknowledge important discussions with F. Lecocq. We also acknowledge the Yale Quantum Institute. Any mention of commercial products is for information only; it does not imply recommendation or endorsement by NIST. The use of facilities is supported by the Yale SEAS clean room and YINQE. This research is supported by AFOSR under Grant No. PFA9550-15-1-0029 and by ARO under Grants No. W911NF- 18-1-0212 and No. W911NF-18-1-0020.


## APPENDIX A: DESCRIPTION OF THE DEVICES AND MEASUREMENT SETUP

The device properties are summarized in Table I. The geometric parameters of the SNAIL, the fabrication process, the chip layout, and the packaging are similar to those in Appendix A of Ref. [28]. A schematic of the cryogenic microwave measurement setup used in this experiment is shown in Fig. 5. All measurements are performed using various measurement classes of Keysight PNA-X N5242A network analyzer.

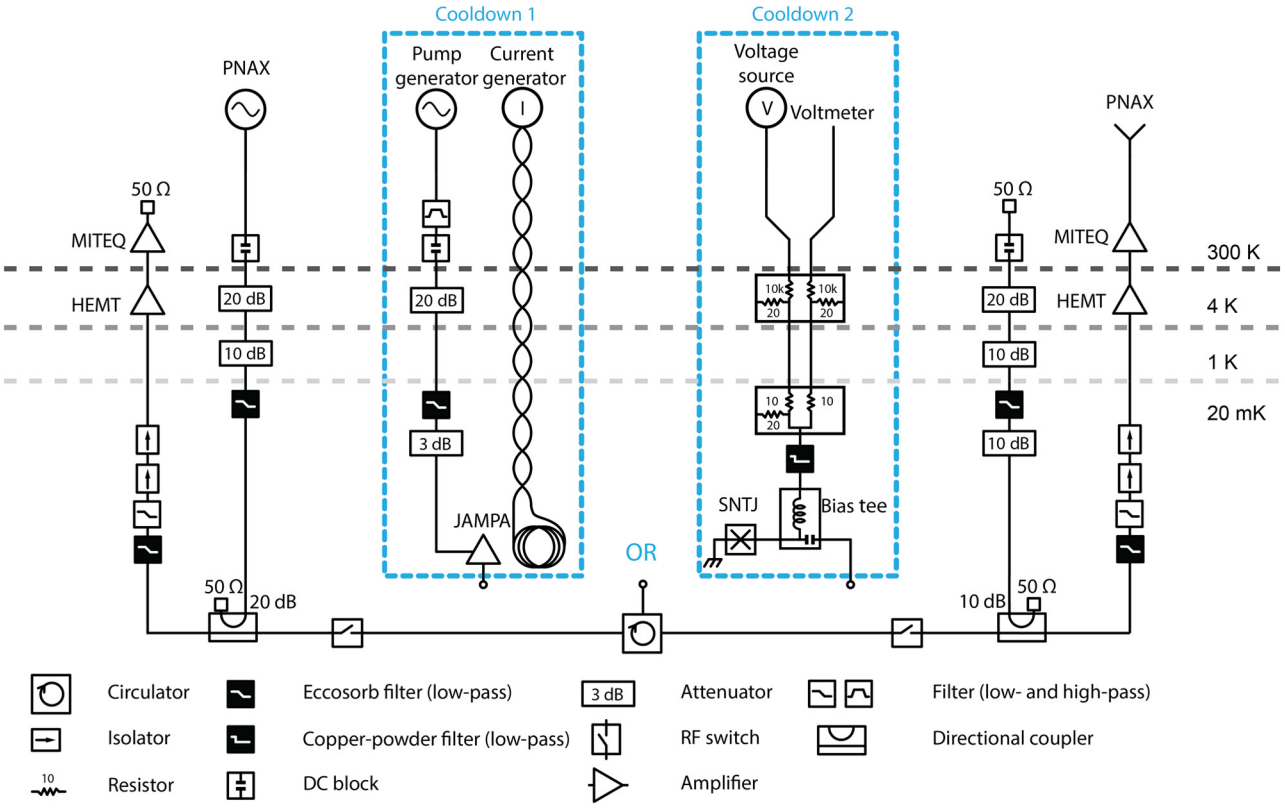


FIG. 5. Schematic of the cryogenic microwave measurement setup used in this experiment. The extra input and output lines and rf switches are used in other experiments not described in this paper. The parts of the setup enclosed in blue boxes are connected to the circulator port in two separate cooldowns.

## APPENDIX B: EIGENMODE DECOMPOSITION AND NONLINEARITIES OF THE JAMPA

In this appendix, we derive the mode structure of the system shown in Fig. 2(a), treating both the transmission-line resonator and the array in a continuous approximation.

### 1. The SNAIL

In this section, we provide a brief description of the properties of the SNAIL, and refer to Refs. [28,29] for more details. The potential energy of a SNAIL with a junction inductance ratio $\alpha$ can be written as

$$U_S(\varphi) = -E_J\left[\alpha\cos\varphi + 3\cos\left(\frac{\varphi_{\text{ext}}-\varphi}{3}\right)\right], \tag{B1}$$

where $\varphi$ is the phase across the small junction of the SNAIL, $\varphi_{\text{ext}} = \Phi/\phi_0$, and $\phi_0 = \hbar/2e$ is the reduced flux quantum. Introducing the generalized flux $\Delta\phi = \phi_0\varphi$ and expanding the potential around the minimum $\phi_{\min}$, we obtain

$$U_S = \frac{(\Delta\phi-\phi_{\min})^2}{2L_S(\Phi)} + E_J\sum_{n=3}^{\infty}\frac{c_n(\Phi)}{n!\phi_0^n}(\Delta\phi-\phi_{\min})^n, \tag{B2}$$

where $L_S(\Phi) = L_J/c_2(\Phi)$ is the flux-dependent linear inductance, and the Taylor expansion coefficients $c_n(\Phi)$ depend only on $\Phi$ and the fixed asymmetry coefficient $\alpha$. Note that any other inductive circuit element shown in Fig. 2(b) can be incorporated into the formalism of this section by appropriately changing the expansion coefficients $c_n$ and the location of the potential minimum $\phi_{\min}$.

In the continuous model, we replace $\Delta\phi$ by $a\partial_x\phi$ and absorb the gradiometric flux offset into the definition of $\phi$: $\phi - (x/a)\phi_{\min} \to \phi$.

### 2. Resonant frequencies

Let us denote the capacitance and inductance per unit length of the transmission-line resonator by $c_r$ and $\ell_r$, respectively. Then the characteristic impedance is given by $Z_c = \sqrt{\ell_r/c_r}$, and the phase velocity is given by $v_r = 1/\sqrt{\ell_r c_r}$. Similarly, for a SNAIL array with a unit cell of size $a$, the capacitance to ground and inductance per unit length are $c_0 = C_0/a$ and $\ell_S(\Phi) = L_S(\Phi)/a$, respectively, and the shunting capacitance of the unit cell is $c_S = C_S a$. With these definitions, we can write the Lagrangian of a linearized system as

$$\mathcal{L} = \left(\int_{-d_1/2}^{-d_0/2} + \int_{d_0/2}^{d_1/2}\right)\left[\frac{c_r}{2}(\partial_t\phi)^2 - \frac{1}{2\ell_r}(\partial_x\phi)^2\right]dx + \int_{-d_0/2}^{d_0/2}\left[\frac{c_0}{2}(\partial_t\phi)^2 + \frac{c_S}{2}(\partial_x\partial_t\phi)^2 - \frac{1}{2\ell_S}(\partial_x\phi)^2\right]dx, \tag{B3}$$

where $d_0 = Ma$ is the total array size and $d_1 = Ma + 2d_r$ is the total size of the device. By varying the action for this Lagrangian, we can find the Lagrange equations of motion of the flux field $\phi(x,t)$:

(a) In the transmission-line resonator,

$$-c_r\partial_t^2\phi + \frac{1}{\ell_r}\partial_x^2\phi = 0; \tag{B4}$$

(b) In the SNAIL array,

$$-c_0\partial_t^2\phi + c_S\partial_x^2\partial_t^2\phi + \frac{1}{\ell_S}\partial_x^2\phi = 0. \tag{B5}$$

In addition, this procedure yields the continuity conditions at the various boundaries of the system: (i) a zero-current boundary condition at the ends of the transmission line,

$$\begin{aligned}\partial_x\phi\big|_{x=-d_1/2} &= 0,\\ \partial_x\phi\big|_{x=+d_1/2} &= 0;\end{aligned} \tag{B6}$$

(ii) a current continuity condition at the points connecting the transmission-line resonator and the array,

$$\begin{aligned}\frac{1}{\ell_r}\partial_x\phi\Big|_{x=-d_0/2-0} &= \left(\frac{1}{\ell_S}\partial_x\phi + c_S\partial_x\partial_t^2\phi\right)\Big|_{x=-d_0/2+0},\\ \frac{1}{\ell_r}\partial_x\phi\Big|_{x=+d_0/2+0} &= \left(\frac{1}{\ell_S}\partial_x\phi + c_S\partial_x\partial_t^2\phi\right)\Big|_{x=+d_0/2-0};\end{aligned} \tag{B7}$$

and (iii) a flux (or voltage) continuity condition at the points connecting the transmission-line resonator and the array,

$$\begin{aligned}\phi\big|_{x=-d_0/2-0} &= \phi\big|_{x=-d_0/2+0},\\ \phi\big|_{x=+d_0/2+0} &= \phi\big|_{x=+d_0/2-0}.\end{aligned} \tag{B8}$$

Because we neglect the nonlinearity of the SNAIL, all the equations of motion obtained are linear and can be solved analytically. We look for a harmonic solution corresponding to the eigenfrequency $\omega$ in the piecewise form

$$\phi = \begin{cases} A_-\cos k_r x + B_-\sin k_r x, & x < -d_0/2,\\ A_S\cos k_S x + B_S\sin k_S x, & |x| < d_0/2,\\ A_+\cos k_r x + B_+\sin k_r x, & x > d_0/2,\end{cases} \tag{B9}$$

where the wave vectors $k_r$ (in the resonator) and $k_S$ (in the array) are related to the frequency $\omega$ via

$$\omega^2 = \frac{1}{\ell_r c_r}k_r^2, \tag{B10}$$

$$\omega^2 = \frac{1}{\ell_S c_S}\frac{k_S^2}{k_S^2 + c_0/c_S}, \tag{B11}$$

which follows from Eqs. (B4) and (B5) in the Fourier domain. By substituting the ansatz solution given by Eq. (B9) into Eqs. (B6)–(B8), we obtain a system of six linear equations to determine the amplitudes $(A_- \; B_- \; A_S \; B_S \; A_+ \; B_+)^T$. The eigenmode frequencies of the system can be determined by requiring that the determinant of this system of equations is zero, while the eigenvectors provide the spatial profile of the eigenmode flux distribution. The equation for the determinant of the system can be factorized and solved separately for the odd and even modes,

$$\tan\left(\frac{d_r\omega}{v_r}\right)\tan\left(\frac{M\omega}{2\omega_0\sqrt{1-\omega^2/\omega_p^2}}\right)=\frac{Z_c}{Z_S}\sqrt{1-\frac{\omega^2}{\omega_p^2}}, \tag{B12}$$

$$\tan\left(\frac{d_r\omega}{v_r}\right)\cot\left(\frac{M\omega}{2\omega_0\sqrt{1-\omega^2/\omega_p^2}}\right)=-\frac{Z_c}{Z_S}\sqrt{1-\frac{\omega^2}{\omega_p^2}}, \tag{B13}$$

where we introduce the "plasma frequency" $\omega_p = 1/\sqrt{L_S C_S}$, the characteristic impedance of the SNAIL transmission line $Z_S = \sqrt{L_S/C_S}$, and $\omega_0 = 1/\sqrt{L_S C_0}$. Equations (B12) and (B13) can be solved numerically to yield the resonance frequencies $\omega_n$ of the array modes. In order to produce Fig. 2(c), we fix the fundamental mode at the desired operating frequency $\omega_{\rm op}$, and the corresponding length of the resonator pads has to be determined from

$$d_r=\frac{v_r}{\omega_{\rm op}}\arctan\left\{\frac{Z_c}{Z_S}\sqrt{1-\frac{\omega_{\rm op}^2}{\omega_p^2}}\cot\left(\frac{M\omega_{\rm op}}{2\omega_0\sqrt{1-\omega_{\rm op}^2/\omega_p^2}}\right)\right\}. \tag{B14}$$

The critical value $M = M_c$, after which the resonator pads shrink to zero and we lose the use of $d_r$ as a frequency-controlling knob, is given by

$$M_c=\pi\frac{\omega_0}{\omega_{\rm op}}\sqrt{1-\frac{\omega_{\rm op}^2}{\omega_p^2}}. \tag{B15}$$

For $M > M_c$, we can simplify Eqs. (B12) and (B13) and obtain a closed-form solution for the mode frequencies of the array,

$$\omega_n=\frac{\omega_p}{\sqrt{1+\left(M\omega_p/\pi n\omega_0\right)^2}}. \tag{B16}$$

It is clear from this equation that the frequencies $\omega_n$ of the low-lying modes are approximately equally spaced, with $\Delta\omega \approx \pi\omega_0/M$.

### 3. Participation ratio

It is helpful to know how the participation of the array changes with $M$, as this controls characteristic features of the dependence of the resonant frequency and the self-Kerr nonlinearity on $M$. We can use the solution $\phi(x)$ of the linearized system to define the inductive EPR as

$$p=\frac{\int_{-d_0/2}^{d_0/2}[(\partial_x\phi)^2/2\ell_S]\,dx}{\left(\int_{-d_1/2}^{-d_0/2}+\int_{d_0/2}^{d_1/2}\right)[(\partial_x\phi)^2/2\ell_r]\,dx+\int_{-d_0/2}^{d_0/2}[(\partial_x\phi)^2/2\ell_S]\,dx}. \tag{B17}$$

The dependence of the EPR on the number of unit cells $M$ in the array is shown in Fig. 6. In general, this dependence is nonmonotonic, showing that the mode structure changes in a nontrivial way.

We can identify a few features that are nevertheless easy to correlate with Figs. 2(c) and 2(d). In particular, the linear increase in the self-Kerr nonlinearity at small $M$, as predicted by Eq. (3), relies on the EPR of the unit cell being independent of $M$. This condition is confirmed in Fig. 6(b), where the saturation of $p/M$ at $p_J \approx 0.033$ is apparent. In contrast, at large $M$ the participation ratio becomes 1 by definition, and its per-unit value decreases as $1/M$, leading to dilution of the nonlinearity in the JAMPA. Note that in reality $p$ would saturate at a value smaller than 1 because of the spurious inductance of the leads within the circuit of a SNAIL unit cell. Our model does not account for this effect, although it becomes significant when the geometric inductance of the SNAIL loop is comparable to $L_J$.

The separation of the diagram in Fig. 2(c) into four regions roughly corresponds to where the EPR per unit cell (I) stays approximately constant, (II) reduces to half its asymptotic value, (III) crosses over into a $1/M$ dependence, and (IV) becomes strictly equal to $1/M$.

### 4. Self-Kerr nonlinearities

After solving the linearized system, we proceed to study the nonlinearities. In general, the Hamiltonian obtained after eigenmode decomposition contains nonlinear couplings of all orders and between all modes. Therefore it can be written as

$$H=\sum_n\omega_n a_n^\dagger a_n+\sum_{ijk}g_3^{(ijk)}(a_i+a_i^\dagger)(a_j+a_j^\dagger)(a_k+a_k^\dagger)+\sum_{ijkl}g_4^{(ijkl)}(a_i+a_i^\dagger)(a_j+a_j^\dagger)(a_k+a_k^\dagger)(a_l+a_l^\dagger)+\cdots. \tag{B18}$$

Our goal is to establish the characteristic scaling of the nonlinearities with $M$, and therefore we make a few simplifying assumptions. First, we focus on $\Phi = 0$. In this case all odd nonlinearities vanish due to the inversion symmetry, and the amplifier cannot be used in the three-wave mixing mode at this particular external magnetic

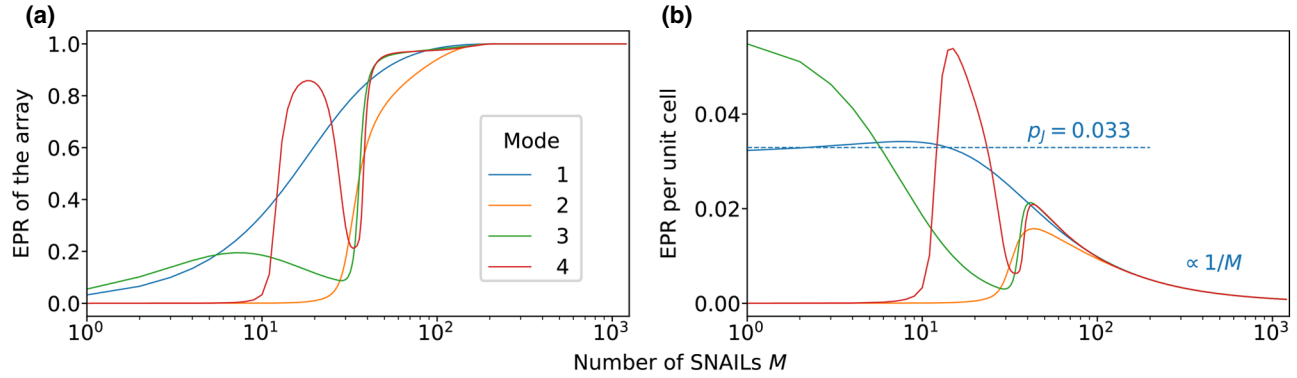


FIG. 6. (a) Inductive energy participation ratio $p$ of the array with respect to the total inductive energy of the mode, based on the quadratic approximation. (b) EPR scaled by the number of unit cells in the array.

flux. However, the method presented here can be extended easily to calculate any coupling $g_3^{(ijk)}$ at an arbitrary flux. Second, we calculate only the self-Kerr nonlinearities $K_n \equiv 12g_4^{(nnnn)}$. We expect that this linear participation-ratio-based method would need to be significantly modified in order to calculate the Kerr nonlinearity at nonzero flux, due to corrections from the third-order coefficient in the potential energy of the SNAIL, as was shown in Refs. [28,29]. However, we note that this method can still be applied easily at nonzero flux for systems in which the Kerr nonlinearity is the lowest-order nonlinearity, such as arrays of Josephson junctions or SQUIDs.

According to the black-box quantization method [57], after the linearized problem is solved, the nonlinearity can be simply applied to the linear flux distribution found in Eq. (B9). For the SNAIL array at $\Phi = 0$, the fourth-order nonlinear contribution to the Hamiltonian is given by

$$U_{\mathrm{NL}} = \frac{1}{a}\int_{-d_0/2}^{+d_0/2} \frac{c_4}{4!L_J\phi_0^2}(a\partial_x\phi)^4\,dx. \tag{B19}$$

Next, we plug in the flux distribution (B9) and integrate over $x$, which leads to quartic nonlinear couplings between the amplitudes $A_S$ and $B_S$ of the various modes. Since we are interested only in the self-Kerr nonlinearities $K_n$, we select only the terms in the potential energy $U_{\mathrm{NL}}$ that are related to the mode $n$. These potential-energy terms have the form

$$U_n = \frac{c_4}{4!L_J\phi_0^2}\frac{(ak_S)^3}{16}\left[6(A_S^2+B_S^2)^2(d_0k_S) + 8(-A_S^4+B_S^4)\right.$$
$$\left.\times\sin(d_0k_S) + (A_S^4 - 6A_S^2B_S^2 + B_S^4)\sin(2d_0k_S)\right]. \tag{B20}$$

Note that the amplitudes $A_S$ and $B_S$ are not independent, and the relation between them is established when the eigenvalue problem is solved for the system of equations (B6)–(B8).

In general this is a cumbersome, albeit straightforward, procedure which is much easier done numerically, but we present here the outline of the actions for the easily solvable case of $d_r = 0$. In this case the dispersion relation has the form of Eq. (B16). The open boundary condition (B6) leads to the dimensional quantization of the wave vector $k_S^{(n)} = (\pi/a)(n/M)$, and the eigenmodes have a simple structure with $A_S = 0$ for odd modes and $B_S = 0$ for even modes. Given this, the contribution to the Hamiltonian from mode $n$ simplifies to

$$H_n = \left(\frac{C_0M}{4} + \frac{C_SM(ak_S^{(n)})^2}{4}\right)\dot{D}^2 + \frac{(ak_S^{(n)})^2M}{4L_S}D^2$$
$$+ \frac{c_4}{4!L_S\phi_0^2}\frac{3}{8}(ak_S^{(n)})^4MD^4, \tag{B21}$$

where $D$ can be either $A_S$ or $B_S$, depending on the parity of the mode. After applying canonical quantization, this can be transformed to

$$H_n = \omega_n a_n^\dagger a_n + \frac{1}{12}K_n(a_n + a_n^\dagger)^4, \tag{B22}$$

with $\omega_n$ given by Eq. (B16) and $K_n$ given by

$$K_n = \frac{3}{16}\frac{c_4}{c_2}\frac{L_S}{M\phi_0^2}\omega_n^2. \tag{B23}$$

Note that the Hamiltonian is not simply a sum of terms of the type (B22), since it also contains cross-Kerr couplings between all modes.

Although the more general case with $d_r \neq 0$ can also be treated analytically, the expressions obtained are cumbersome and do not provide much insight. Instead, we solve the general case numerically and present the results in Fig. 2(d). For the numerics, we use the following realistic system parameters: $\omega_{\mathrm{op}} = 8$ GHz, $C_0 = 0.71$ fF, $C_S = 0.11$ pF, $L_S = 110$ pH, $Z_c = 46\,\Omega$, and $v_r = 1.2\times10^8$ m/s.

## APPENDIX C: NOISE CALIBRATION

We calibrate the noise temperature of the JAMPA, $T_N$, and its 1-dB compression point, $P_{1\,\mathrm{dB}}$, shown in Figs. 4(d) and 4(f), using a SNTJ [45,46]. The noise emitted from the SNTJ, amplified by the full cryogenic and room-temperature measurement chain, has the following power spectrum:

$$P_N(\omega) = G_{\mathrm{sys}}(\omega)k_B B\left[T_{\mathrm{sys}}(\omega) + \frac{1}{2}\left(\frac{eV+\hbar\omega}{2k_B}\right)\coth\left(\frac{eV+\hbar\omega}{2k_BT}\right) + \frac{1}{2}\left(\frac{eV-\hbar\omega}{2k_B}\right)\coth\left(\frac{eV-\hbar\omega}{2k_BT}\right)\right], \tag{C1}$$

where $G_{\mathrm{sys}}(\omega)$ is the frequency-dependent system gain, $T_{\mathrm{sys}}(\omega)$ is the frequency-dependent system noise temperature (without the parametric amplifier), $T$ is the junction temperature, $V$ is the voltage applied across the junction, $B$ is the resolution bandwidth over which noise is collected, and $k_B$ and $\hbar$ are the Boltzmann and Planck constants. We use the high-voltage limit of this expression,

$$P_N(\omega) = G_{\mathrm{sys}}(\omega)k_B B\left[T_{\mathrm{sys}}(\omega) + \frac{e|V|}{2k_B}\right], \tag{C2}$$

which allows for simple extraction of $G_{\mathrm{sys}}(\omega)$ and $T_{\mathrm{sys}}(\omega)$ using linear fits.

To extract $T_N$, we mount the JAMPA in place of the SNTJ and measure the noise visibility ratio (NVR). $T_N$ is extracted from

$$\mathrm{NVR} = \frac{G_{\mathrm{sys}}[T_{\mathrm{sys}} + G(T_Q + T_N)]}{G_{\mathrm{sys}}(T_{\mathrm{sys}} + T_Q)}, \tag{C3}$$

where $G$ is the gain of the JAMPA and $T_Q = \hbar\omega/2k_B$. The SQL corresponds to $T_N = T_Q$.

Following this outline, we measure $T_{\mathrm{sys}}(\omega)$ and $G_{\mathrm{sys}}(\omega)$, shown in Fig. 7, in a separate cooldown, after mounting the SNTJ in the same place as the JAMPA. The total gain of the chain in this case includes contributions from the high-electron-mobility transistor (HEMT) amplifier mounted in the 4 K stage of the dilution refrigerator and the MITEQ amplifier at room temperature. The increased system noise compared with the factory specifications of the HEMT (model LNF-LNC4-16) results from the attenuation between the HEMT and the SNTJ, and is typical of such setups [8,39,43].

The error bars on $T_{\mathrm{sys}}$ and $T_N$ result from three major possible systematic errors:

(i) The finite $S_{11}$ of the SNTJ means that not all noise power is collected due to the impedance mismatch. This effect leads to an overestimation of $T_N$, which gets worse at higher frequencies when the on-chip resonance of the SNTJ at about 11.5 GHz is approached.

(ii) A possible miscalibration of the voltage across the SNTJ due to the change in the ratio of the resistive voltage divider at low temperature. This error is symmetric and estimated to be about $\pm 10\%$.

(iii) A shift of the calibration reference plane due to the bias tee used with the SNTJ. This effect was studied in detail in Ref. [58]: it can be modeled as a beam splitter that mixes the voltage-dependent noise of the SNTJ with the (presumably quantum) noise of the bias tee. This causes the SNTJ to report a higher system noise temperature and smaller gain according to

$$G'_{\mathrm{sys}} = \eta G_{\mathrm{sys}}, \quad T'_{\mathrm{sys}} = \frac{1}{\eta}T_{\mathrm{sys}} + \frac{1-\eta}{\eta}T_Q, \tag{C4}$$

where $\eta \approx -0.6$ dB is the insertion loss of the bias tee measured at room temperature. We account for the finite $\eta$ in the noise calibration. We note, however, that $\eta$ can increase when the bias tee is cooled down, which would increase $T_N$ by up to 10% (corresponding to $\eta = 1$).

Other sources of error, such as the statistical error of the fit and the error due to measuring the SNTJ in a separate cooldown, are insignificant in comparison.

Knowing $G_{\mathrm{sys}}(\omega)$, we can also calibrate the absolute power in the device plane, which determines $P_{1\,\mathrm{dB}}$. We find that this value is on average 2.3 dB higher than that extracted with knowledge of the input-line attenuation when the dilution refrigerator is warm; this difference is consistent with the fact that the line attenuation reduces slightly at low temperature.

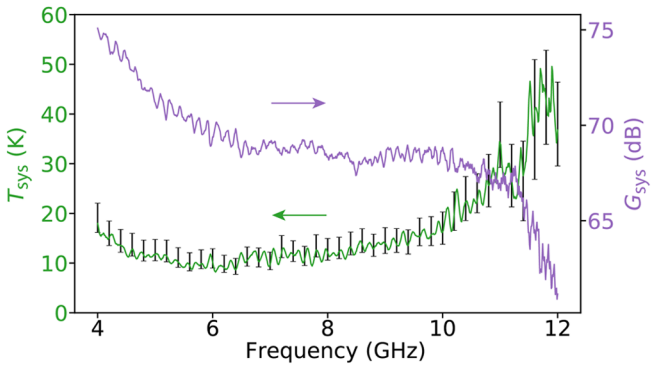


FIG. 7. System noise temperature $T_{\mathrm{sys}}(\omega)$ and gain $G_{\mathrm{sys}}(\omega)$ of the amplification chain measured using a SNTJ mounted in place of the JAMPA.

[1] N. Ofek, A. Petrenko, R. Heeres, P. Reinhold, Z. Leghtas, B. Vlastakis, Y. Liu, L. Frunzio, S. M. Girvin, and L. Jiang, *et al.*, Extending the lifetime of a quantum bit with error correction in superconducting circuits, Nature **536**, 441 (2016).

[2] P. Campagne-Ibarcq, A. Eickbusch, S. Touzard, E. Zalys-Geller, N. E. Frattini, V. V. Sivak, P. Reinhold, S. Puri, S. Shankar, and R. J. Schoelkopf *et al.*, A stabilized logical quantum bit encoded in grid states of a superconducting cavity, arXiv:1907.12487 (2019).

[3] A. A. Houck, J. A. Schreier, B. R. Johnson, J. M. Chow, J. Koch, J. M. Gambetta, D. I. Schuster, L. Frunzio, M. H. Devoret, and S. M. Girvin, *et al.*, Controlling the Spontaneous Emission of a Superconducting Transmon Qubit, Phys. Rev. Lett. **101**, 080502 (2008).

[4] J. J. Burnett, A. Bengtsson, M. Scigliuzzo, D. Niepce, M. Kudra, P. Delsing, and J. Bylander, Decoherence benchmarking of superconducting qubits, npj Quantum Inf. **5**, 54 (2019).

[5] A. Eddins, S. Schreppler, D. M. Toyli, L. S. Martin, S. Hacohen-Gourgy, L. C. G. Govia, H. Ribeiro, A. A. Clerk, and I. Siddiqi, Stroboscopic Qubit Measurement with Squeezed Illumination, Phys. Rev. Lett. **120**, 040505 (2018).

[6] A. Eddins, J. M. Kreikebaum, D. M. Toyli, E. M. Levenson-Falk, A. Dove, W. P. Livingston, B. A. Levitan, L. C. G. Govia, A. A. Clerk, and I. Siddiqi, High-Efficiency Measurement of an Artificial Atom Embedded in a Parametric Amplifier, Phys. Rev. X **9**, 011004 (2019).

[7] E. Flurin, N. Roch, F. Mallet, M. H. Devoret, and B. Huard, Generating Entangled Microwave Radiation Over Two Transmission Lines, Phys. Rev. Lett. **109**, 183901 (2012).

[8] C. W. Sandbo Chang, M. Simoen, J. Aumentado, C. Sabín, P. Forn-Díaz, A. M. Vadiraj, F. Quijandría, G. Johansson, I. Fuentes, and C. M. Wilson, Generating Multimode Entangled Microwaves with a Superconducting Parametric Cavity, Phys. Rev. Appl. **10**, 044019 (2018).

[9] M. A. Castellanos-Beltran, K. D. Irwin, G. C. Hilton, L. R. Vale, and K. W. Lehnert, Amplification and squeezing of quantum noise with a tunable Josephson metamaterial, Nat. Phys. **4**, 929 (2008).

[10] T. Yamamoto, K. Inomata, M. Watanabe, K. Matsuba, T. Miyazaki, W. D. Oliver, Y. Nakamura, and J. S. Tsai, Flux-driven Josephson parametric amplifier, Appl. Phys. Lett. **93**, 042510 (2008).

[11] N. Bergeal, F. Schackert, M. Metcalfe, R. Vijay, V. E. Manucharyan, L. Frunzio, D. E. Prober, R. J. Schoelkopf, S. M. Girvin, and M. H. Devoret, Phase-preserving amplification near the quantum limit with a Josephson ring modulator, Nature **465**, 64 (2010).

[12] B. Abdo, A. Kamal, and M. Devoret, Nondegenerate three-wave mixing with the Josephson ring modulator, Phys. Rev. B **87**, 014508 (2013).

[13] K. O'Brien, C. Macklin, I. Siddiqi, and X. Zhang, Resonant Phase Matching of Josephson Junction Traveling Wave Parametric Amplifiers, Phys. Rev. Lett. **113**, 157001 (2014).

[14] C. Macklin, K. O'Brien, D. Hover, M. E. Schwartz, V. Bolkhovsky, X. Zhang, W. D. Oliver, and I. Siddiqi, A near-quantum-limited Josephson traveling-wave parametric amplifier, Science **350**, 307 (2015).

[15] M. T. Bell and A. Samolov, Traveling-Wave Parametric Amplifier Based on a Chain of Coupled Asymmetric SQUIDs, Phys. Rev. Appl. **4**, 024014 (2015).

[16] T. C. White, J. Y. Mutus, I.-C. Hoi, R. Barends, B. Campbell, Y. Chen, Z. Chen, B. Chiaro, A. Dunsworth, and E. Jeffrey, *et al.*, Traveling wave parametric amplifier with Josephson junctions using minimal resonator phase matching, Appl. Phys. Lett. **106**, 242601 (2015).

[17] A. B. Zorin, Josephson Traveling-Wave Parametric Amplifier with Three-Wave Mixing, Phys. Rev. Appl. **6**, 034006 (2016).

[18] L. Planat, A. Ranadive, R. Dassonneville, J. P. Martinez, S. Leger, C. Naud, O. Buisson, W. Hasch-Guichard, D. M. Basko, and N. Roch, A photonic crystal Josephson traveling wave parametric amplifier, arXiv:1907.10158 (2019).

[19] B. Ho Eom, P. K. Day, H. G. LeDuc, and J. Zmuidzinas, A wideband, low-noise superconducting amplifier with high dynamic range, Nat. Phys. **8**, 623 (2012).

[20] M. R. Vissers, R. P. Erickson, H.-S. Ku, L. Vale, X. Wu, G. C. Hilton, and D. P. Pappas, Low-noise kinetic inductance traveling-wave amplifier using three-wave mixing, Appl. Phys. Lett. **108**, 012601 (2016).

[21] S. Chaudhuri, D. Li, K. D. Irwin, C. Bockstiegel, J. Hubmayr, J. N. Ullom, M. R. Vissers, and J. Gao, Broadband parametric amplifiers based on nonlinear kinetic inductance artificial transmission lines, Appl. Phys. Lett. **110**, 152601 (2017).

[22] L. Ranzani, M. Bal, K. C. Fong, G. Ribeill, X. Wu, J. Long, H.-S. Ku, R. P. Erickson, D. Pappas, and T. A. Ohki, Kinetic inductance traveling-wave amplifiers for multiplexed qubit readout, Appl. Phys. Lett. **113**, 242602 (2018).

[23] N. Zobrist, B. H. Eom, P. Day, B. A. Mazin, S. R. Meeker, B. Bumble, H. G. LeDuc, G. Coiffard, P. Szypryt, and N. Fruitwala *et al.*, Wide-band parametric amplifier readout and resolution of optical microwave kinetic inductance detectors, arXiv:1907.03078 (2019).

[24] J. Heinsoo, C. K. Andersen, A. Remm, S. Krinner, T. Walter, Y. Salathé, S. Gasparinetti, J.-C. Besse, A. Potočnik, and A. Wallraff*et al.*, Rapid High-Fidelity Multiplexed Readout of Superconducting Qubits, Phys. Rev. Appl. **10**, 034040 (2018).

[25] C. C. Bultink, B. Tarasinski, N. Haandbæk, S. Poletto, N. Haider, D. J. Michalak, A. Bruno, and L. DiCarlo, General method for extracting the quantum efficiency of dispersive qubit readout in circuit QED, Appl. Phys. Lett. **112**, 092601 (2018).

[26] S. Krinner, S. Storz, P. Kurpiers, P. Magnard, J. Heinsoo, R. Keller, J. Lütolf, C. Eichler, and A. Wallraff, Engineering cryogenic setups for 100-qubit scale superconducting circuit systems, EPJ Quantum Technol. **6**, 2 (2019).

[27] T. Peronnin, D. Marković, Q. Ficheux, and B. Huard, Sequential measurement of a superconducting qubit, arXiv:1904.04635 (2019).

[28] V. V. Sivak, N. E. Frattini, V. R. Joshi, A. Lingenfelter, S. Shankar, and M. H. Devoret, Kerr-Free Three-Wave Mixing in Superconducting Quantum Circuits, Phys. Rev. Appl. **11**, 054060 (2019).

[29] N. E. Frattini, V. V. Sivak, A. Lingenfelter, S. Shankar, and M. H. Devoret, Optimizing the Nonlinearity and Dissipation of a SNAIL Parametric Amplifier for Dynamic Range, Phys. Rev. Appl. **10**, 054020 (2018).

[30] P. Winkel, I. Takmakov, D. Rieger, L. Planat, W. Hasch-Guichard, L. Grünhaupt, N. Maleeva, F. Foroughi, F. Henriques, K. Borisov *et al.*, Nondegenerate Parametric Amplifiers Based on Dispersion-Engineered Josephson-Junction Arrays, Phys. Rev. Appl. **13**, 024015 (2020).

[31] G. Liu, T.-C. Chien, X. Cao, O. Lanes, E. Alpern, D. Pekker, and M. Hatridge, Josephson parametric converter saturation and higher order effects, Appl. Phys. Lett. **111**, 202603 (2017).

[32] L. Planat, R. Dassonneville, J. P. Martínez, F. Foroughi, O. Buisson, W. Hasch-Guichard, C. Naud, R. Vijay, K. Murch, and N. Roch, Understanding the Saturation Power of Josephson Parametric Amplifiers Made from SQUID Arrays, Phys. Rev. Appl. **11**, 034014 (2019).

[33] K. O'Brien, Private communication.

[34] C. Eichler and A. Wallraff, Controlling the dynamic range of a Josephson parametric amplifier, EPJ Quantum Technol. **1**, 2 (2014).

[35] N. A. Masluk, I. M. Pop, A. Kamal, Z. K. Minev, and M. H. Devoret, Microwave Characterization of Josephson Junction Arrays: Implementing a Low Loss Superinductance, Phys. Rev. Lett. **109**, 137002 (2012).

[36] V. E. Manucharyan, Ph.D. thesis, School Yale University, 2012.

[37] Z. K. Minev, Ph.D. thesis, School Yale University, 2019.

[38] X. Zhou, V. Schmitt, P. Bertet, D. Vion, W. Wustmann, V. Shumeiko, and D. Esteve, High-gain weakly nonlinear flux-modulated Josephson parametric amplifier using a SQUID array, Phys. Rev. B. **89**, 214517 (2014).

[39] T. Roy, S. Kundu, M. Chand, A. M. Vadiraj, A. Ranadive, N. Nehra, M. P. Patankar, J. Aumentado, A. A. Clerk, and R. Vijay, Broadband parametric amplification with impedance engineering: Beyond the gain-bandwidth product, Appl. Phys. Lett. **107**, 262601 (2015).

[40] Y. Krupko, V. D. Nguyen, T. Weißl, É. Dumur, J. Puertas, R. Dassonneville, C. Naud, F. W. J. Hekking, D. M. Basko, and O. Buisson, *et al.*, Kerr nonlinearity in a superconducting Josephson metamaterial, Phys. Rev. B. **98**, 094516 (2018).

[41] M. Hays, V. Fatemi, K. Serniak, D. Bouman, S. Diamond, G. de Lange, P. Krogstrup, J. Nygård, A. Geresdi, and M. H. Devoret, Continuous monitoring of a trapped, superconducting spin, arXiv:1908.02800 (2019).

[42] T. Weißl, S. W. Jolin, R. Borgani, D. Forchheimer, and D. B. Haviland, A general characterization method for nonlinearities in superconducting circuits, New J. Phys. **21**, 053018 (2019).

[43] M. Simoen, C. W. S. Chang, P. Krantz, J. Bylander, W. Wustmann, V. Shumeiko, P. Delsing, and C. M. Wilson, Characterization of a multimode coplanar waveguide parametric amplifier, J. Appl. Phys. **118**, 154501 (2015).

[44] As was shown in [28,31], the saturation of JPAs sometimes leads to a sharp increase in gain with increased signal power. In [31], it was suggested that one should distinguish between the $+1$- and $-1$-dB compression points to capture this effect.

[45] L. Spietz, K. Lehnert, I. Siddiqi, and R. J. Schoelkopf, Primary electronic thermometry using the shot noise of a tunnel junction, Science **300**, 1929 (2003).

[46] L. Spietz, K. Irwin, M. Lee, and J. Aumentado, Noise performance of lumped element direct current superconducting quantum interference device amplifiers in the 4–8 GHz range, Appl. Phys. Lett. **97**, 142502 (2010).

[47] C. M. Caves, Quantum limits on noise in linear amplifiers, Phys. Rev. D **26**, 1817 (1982).

[48] W. Wustmann and V. Shumeiko, Parametric effects in circuit quantum electrodynamics, Low Temp. Phys. **45**, 848 (2019).

[49] B. Abdo, J. M. Chavez-Garcia, M. Brink, G. Keefe, and J. M. Chow, Time-multiplexed amplification in a hybrid-less and coil-less Josephson parametric converter, Appl. Phys. Lett. **110**, 082601 (2017).

[50] A. Kou, W. C. Smith, U. Vool, I. M. Pop, K. M. Sliwa, M. Hatridge, L. Frunzio, and M. H. Devoret, Simultaneous Monitoring of Fluxonium Qubits in a Waveguide, Phys. Rev. Appl. **9**, 64022 (2018).

[51] M. Jerger, S. Poletto, P. Macha, U. Hübner, E. Il'ichev, and A. V. Ustinov, Frequency division multiplexing readout and simultaneous manipulation of an array of flux qubits, Appl. Phys. Lett. **101**, 042604 (2012).

[52] V. Schmitt, X. Zhou, K. Juliusson, B. Royer, A. Blais, P. Bertet, D. Vion, and D. Esteve, Multiplexed readout of transmon qubits with Josephson bifurcation amplifiers, Phys. Rev. A **90**, 062333 (2014).

[53] S. Kundu, N. Gheeraert, S. Hazra, T. Roy, K. V. Salunkhe, M. P. Patankar, and R. Vijay, Multiplexed readout of four qubits in 3D circuit QED architecture using a broadband Josephson parametric amplifier, Appl. Phys. Lett. **114**, 172601 (2019).

[54] A. L. Grimsmo and A. Blais, Squeezing and quantum state engineering with Josephson travelling wave amplifiers, npj Quantum Inf. **3**, 20 (2017).

[55] N. C. Menicucci, P. van Loock, M. Gu, C. Weedbrook, T. C. Ralph, and M. A. Nielsen, Universal Quantum Computation with Continuous-Variable Cluster States, Phys. Rev. Lett. **97**, 110501 (2006).

[56] O. Naaman, D. G. Ferguson, and R. J. Epstein, High Saturation Power Josephson Parametric Amplifier with GHz Bandwidth, arXiv:1711.07549 (2017).

[57] S. E. Nigg, H. Paik, B. Vlastakis, G. Kirchmair, S. Shankar, L. Frunzio, M. H. Devoret, R. J. Schoelkopf, and S. M. Girvin, Black-Box Superconducting Circuit Quantization, Phys. Rev. Lett. **108**, 240502 (2012).

[58] Su-Wei Chang, J. Aumentado, Wei-Ting Wong, and J. C. Bardin, in *2016 IEEE MTT-S International Microwave Symposium (IMS)* (IEEE, San Francisco, California, USA, 2016), p. 1., ISBN 978-1-5090-0698-4.